Investigating the Eddy Diffusivity Concept in the Coastal Ocean

I. I. RYPINA, A. KIRINCICH, AND S. LENTZ

Woods Hole Oceanographic Institution, Woods Hole, Massachusetts

M. SUNDERMEYER

University of Massachusetts Dartmouth, New Bedford, Massachusetts

(Manuscript received 15 January 2016, in final form 20 April 2016)

ABSTRACT

This paper aims to test the validity, utility, and limitations of the lateral eddy diffusivity concept in a coastal environment through analyzing data from coupled drifter and dye releases within the footprint of a high-resolution (800 m) high-frequency radar south of Martha's Vineyard, Massachusetts. Specifically, this study investigates how well a combination of radar-based velocities and drifter-derived diffusivities can reproduce observed dye spreading over an 8-h time interval. A drifter-based estimate of an anisotropic diffusivity tensor is used to parameterize small-scale motions that are unresolved and underresolved by the radar system. This leads to a significant improvement in the ability of the radar to reproduce the observed dye spreading.

1. Introduction

a. Eddy diffusivity concept

Eddies, commonly defined as deviations from mean flows, play a key role in the redistribution of dynamically and biologically important oceanic quantities such as potential vorticity, heat, salt, and biogeochemical tracers in geophysical flows at scales from submesoscale to that of the ocean basin itself. By analogy with molecular diffusion, the efficiency of eddies in isopycnal tracer transport has been conventionally represented by lateral turbulent or ''eddy'' diffusion. Although this analogy could be questioned for realistic geophysical flows, it provides a simple and effective way to account for the unresolved and underresolved scales of motion in numerical models. As a result, the majority of existing non-eddy-resolving numerical models are diffusion based, often with isotropic diffusivity parameters.

Despite the wide use of the diffusion-based parameterizations, thorough tests of the applicability and limitations of lateral eddy diffusivity concept to real oceanic flows are rare (Kamenkovich et al. 2015), and more work is needed to better understand the validity of diffusion-based parameterizations. In this paper, we make use of data collected during a focused field experiment involving drifters, dye, and a high-resolution (800 m) high-frequency (HF) radar system in the coastal ocean south of Martha's Vineyard, Massachusetts, to examine the nature of eddy diffusivity in a coastal environment. More specifically, we will use a small-scale anisotropic diffusivity tensor derived from real drifter trajectories in combination with larger-scale velocity fields derived from HF radar to predict the observed spreading of dye over the inner part of the continental shelf. Sampled along the actual ship track in the same manner as was done during the field experiment, the predicted dye concentrations were compared to the observed dye concentration to evaluate the utility and limitations of the eddy diffusivity approach in a real coastal ocean setting.

b. Lateral eddy diffusivity estimation using single-particle dispersion tensor

A convenient, although not unique, method for estimating diffusivity is based on calculating the single-particle dispersion for an ensemble of Lagrangian particles relative to their center of mass (e.g., LaCasce 2008; Rypina et al. 2012; Kamenkovich et al. 2015).

Corresponding author address: Irina I. Rypina, Physical Oceanography Department, Woods Hole Oceanographic Institution, Woods Hole, MA 02543.
E-mail: irypina@whoi.edu

DOI: 10.1175/JPO-D-16-0020.1

Alternatively, eddy diffusivities can be obtained by computing the correlation between the velocity and displacement for an ensemble of Lagrangian particles (Davis 1991; Zhurbas and Oh 2004) or by integrating the velocity autocorrelation function (Davis 1991; Sallee et al. 2008; Griesel et al. 2010). Diffusivity can also be estimated based on two-particle (or relative) statistics (LaCasce and Ohlmann 2003; Poje et al. 2014) as well as inferred from the observed or numerically simulated tracer distributions (Sundermeyer and Ledwell 2001; Nakamura 1996, 2001; Abernathey and Marshall 2013). Different methods have different advantages and challenges specific for each technique. Here, we will make use of the single-particle dispersion approach to estimate diffusivity. Following Rypina et al. (2012), the components of the single-particle dispersion tensor for a group of N particles are given by

$$D_{xx}(t;y)=\frac{1}{N}\sum_{n=1}^{N}[\Delta x_n(t)-\Delta X(t)]^2,$$

$$D_{yy}(t;y)=\frac{1}{N}\sum_{n=1}^{N}[\Delta y_n(t)-\Delta Y(t)]^2, \quad \text{and} \tag{1}$$

$$D_{xy}(t;y)=\frac{1}{N}\sum_{n=1}^{N}[\Delta x_n(t)-\Delta X(t)][\Delta y_n(t)-\Delta Y(t)],$$

where, Δx_n and Δy_n are the zonal and meridional displacements, respectively, of the nth particle from its initial position, and $\Delta X(t)=(1/N)\sum_{n=1}^{N}\Delta x_n(t)$ and $\Delta Y(t)=(1/N)\sum_{n=1}^{N}\Delta y_n(t)$ are the ensemble-mean displacements. The dispersion tensor can be diagonalized by rotating the coordinate system by an angle θ such that $\tan 2\theta=[2D_{xy}/(D_{xx}-D_{yy})]$. Physically, θ is the direction of fastest spreading, and diffusivities in this direction (denoted by ξ) and in perpendicular direction (denoted by η) are defined as

$$K_\xi(t)=\frac{1}{2}\frac{\partial D_\xi}{\partial t} \quad \text{and} \quad K_\eta(t)=\frac{1}{2}\frac{\partial D_\eta}{\partial t}, \tag{2}$$

where $D_\xi=D_{xx}\cos^2\theta+D_{xy}\sin 2\theta+D_{yy}\sin^2\theta$, $D_\eta=D_{xx}\sin^2\theta-D_{xy}\sin 2\theta+D_{yy}\cos^2\theta$, and $D_{\xi\eta}=0$.

The shape of the dispersion curve as a function of time contains information about physical processes responsible for the particle spreading. For a purely diffusive regime, such as the random walk process, the dispersion tensor is a linear function of time and the diffusivities in Eq. (2) are constants. However, this random walk–like regime requires that each particle samples many different flow features (such as small-scale eddies, jets, and squirts) and its velocity gets completely uncorrelated from its initial value and from velocities of the neighboring drifters, so that the memory about the previous particle behavior is lost. Under a stochastic velocity disturbance that pushes a particle to take uncorrelated steps in random directions, this regime will occur right away, after just 10 or so random kicks. But in the real ocean, where eddies have nonzero length and time scales, one does not expect the diffusive spreading to settle in immediately, but rather only after some adjustment time interval during which velocities become uncorrelated and drifters lose memory about their past trajectory and trajectories of their neighbors. This adjustment time depends on a particular flow field and generally requires that a drifter samples $O(10)$ independent flow features.

Another distinguished spreading regime that can usually be observed at very small times (much smaller than the onset of diffusive spreading) is ballistic spreading, when the separation between particles or drifters is entirely due to the local velocity shear. In this case, the distance between two drifters grows in proportion to $\Delta\mathbf{v}\cdot t$, where $\Delta\mathbf{v}=\mathbf{v}_1(t)-\mathbf{v}_2(t)$ is the difference in velocity between the drifters. At small enough times, such that the change in the local velocity shear following drifter trajectories can be neglected and one can assume that $\Delta\mathbf{v}\approx$ const, the dispersion, which is the distance squared, will grow in proportion to t^2. Other commonly encountered spreading regimes include the locally dominated Richardson regime ($D\propto t^3$) that occurs in flows where separation at a given scale is controlled by features of a similar scale (Richardson 1926; Bennett 1984; Beron-Vera and LaCasce 2016), and exponential particle separation regime [$D\propto\exp(\alpha t)$] with an exponential separation constant α that occurs in steady linear strain fields or in "chaotic advection flows" with steep kinetic energy spectra (k^{-3} or steeper, where k is the wavenumber) where particle separation at small scales is controlled by larger-scale features (Bennett 1984; Rypina et al. 2010; Beron-Vera and LaCasce 2016). However, given that an exponential can be approximated with a linear term at small times, distinguishing between ballistic and exponential spreading regimes in real data could be challenging. Thus, in this paper we restrict our attention to the diffusive and ballistic regimes, which, as we show below, seem to dominate spreading of the drifters south of Martha's Vineyard over the 8-h experiment.

c. *Parameterizing unresolved motions using scale-dependent and model-specific eddy diffusivities*

There is an implicit flexibility in the choice, meaning, and interpretation of particle displacements Δx_n and Δy_n in Eq. (1) and the resulting diffusivities in Eq. (2). In the most straightforward case, when the total displacements of particles are used, the dispersion of particles is caused by the action of the full flow (i.e., time-mean plus

eddies), and the resulting diffusivities in Eq. (2) quantify the cumulative effect of both the mean and eddy fields on particle spreading. In most applications, however, it is desirable to separate the effects of the mean flow from those of the eddy field, so that the resulting diffusivity can be interpreted as the eddy diffusivity. Specifically, we seek an eddy diffusivity, which quantifies the cumulative effect of eddies that a fluid parcel would feel following its Lagrangian path as it gets advected by the full flow field. In this case, one needs to follow a full trajectory $\mathbf{x}_{\rm tr}(t)$ but, instead of using the full displacements, use the component of the displacement in Eq. (1) that is due to the eddy component of the flow only $\mathbf{u}^{\rm eddy} = \mathbf{u} - \overline{\mathbf{u}}$:

$$\Delta x_n^{\rm eddy}(t) = \int dx_n^{\rm eddy} = \int (dx_n - dx_n^{\rm MeanFlow}) = \int_{t_0}^{t} u^{\rm eddy}[\mathbf{x}_{\rm tr}(t)]\, dt \tag{3}$$

and similarly for the y component. Here, dx_n, $dx_n^{\rm eddy}$, and $dx_n^{\rm MeanFlow}$ are the infinitesimal displacements due to the full, eddy, and mean flow along the full particle trajectory. The $\Delta\mathbf{x}_n^{\rm eddy}(t)$ is sometimes referred to as the pseudotrajectory characterizing the cumulative displacement of a fluid parcel due to the action of the eddy field along the parcel's path as it gets advected by the full flow. Note that this Lagrangian approach is different from the Eulerian approach, where eddy diffusivity is estimated using the "eddy-only" component of the flow and thus characterizes the local effects of eddies at a given geographical location rather than following the Lagrangian particle paths. This technique has been recently used to estimate eddy diffusivities of real and simulated drifters in the North Atlantic (Rypina et al. 2012; Kamenkovich et al. 2015). This method is also equivalent to the eddy diffusivities resulting from integrating the autocorrelation of the Lagrangian velocities along pseudotrajectories (i.e., of the eddy velocity component following full Lagrangian trajectories; Davis 1991; Sallee et al. 2008; Griesel et al. 2010; R. Chen et al. 2014).

With the steady progress in ocean modeling and observing systems, a large part of the eddy field becomes explicitly resolved in modern-day models and observations, so one must parameterize the effects of the unresolved and underresolved eddies only instead of parameterizing the entire eddy field. In this case, the eddy-induced displacements $\Delta\mathbf{x}_n^{\rm eddy}(t)$ and eddy velocities $\mathbf{u}^{\rm eddy}$ in Eq. (3) need to be replaced with their small-scale counterparts $\Delta\mathbf{x}_n^{\rm small}(t)$ and $\mathbf{u}_{\rm small}^{\rm eddy} = \mathbf{u}^{\rm eddy} - \mathbf{u}_{\rm large}^{\rm eddy}$, where the explicitly resolved large-scale velocity has been denoted by $\mathbf{u}_{\rm large}^{\rm eddy}$, leading to

$$\Delta x_n^{\rm small}(t) = \int dx_n^{\rm small} = \int (dx_n - dx_n^{\rm large}) = \int_{t_0}^{t} u^{\rm small}[\mathbf{x}_{\rm tr}(t)]\, dt \tag{4}$$

and similarly for the y component. As above, dx_n, $dx_n^{\rm large}$, and $dx_n^{\rm small}$ are the infinitesimal displacements due to the full flow, large-scale field, and small-scale eddy field along the full particle trajectory $\mathbf{x}_{\rm tr}(t)$. In other words, at each time step following each particle trajectory we subtract the displacement due to the known resolved component of the flow field from the full particle displacement and then integrate (or sum up) the residual displacements to form pseudotrajectories that characterize the cumulative effect of the unresolved and underresolved flow features along the particle path. The corresponding pseudotrajectories given by Eq. (4) can then be analyzed according to Eq. (1) to form the small-scale dispersion tensor, which can be used to compute the small-scale eddy diffusivities via Eq. (2). This small-scale eddy diffusivity quantifies the effects of the unresolved and underresolved motions only and thus should be the most useful for parameterizing these motions in ocean models or observing systems.

While appealing for its practicality and application, like most diffusion-based parameterizations, the approach described above has several rather obvious conceptual challenges. First, the spreading of particles only approaches the diffusive regime after some adjustment time during which the motions of particles become decorrelated, and even then dispersion rarely grows exactly linearly with time. By the time the spreading becomes close to diffusive, most particles are far from their initial location, which leads to the second challenge—nonlocality. The diffusivities estimated using Eqs. (1) and (2) are Lagrangian in nature and thus intrinsically nonlocal. Conversely, the diffusivity K on the right-hand side of the advection–diffusion equation that governs the distribution of a tracer $c(x, y, t)$, $\partial c/\partial t + \mathbf{u}\cdot\nabla c = \nabla\cdot \mathrm{K}\nabla c$, is local and characterizes unresolved eddy effects at a given location, rather than over the larger area assumed in the Lagrangian approach. The third challenge has to do with the large ensemble size of particles (or drifters) that are needed to reliably estimate diffusivities using Eqs. (1) and (2). Finally, when working with real oceanic data obtained from drifters or floats, limitations associated with the not quite Lagrangian nature of drifting/floating instruments, including their inertia, wind slippage, and their constraint to follow the 2D surface flow, present additional challenges for using drifter-based diffusivity estimates for parameterizing

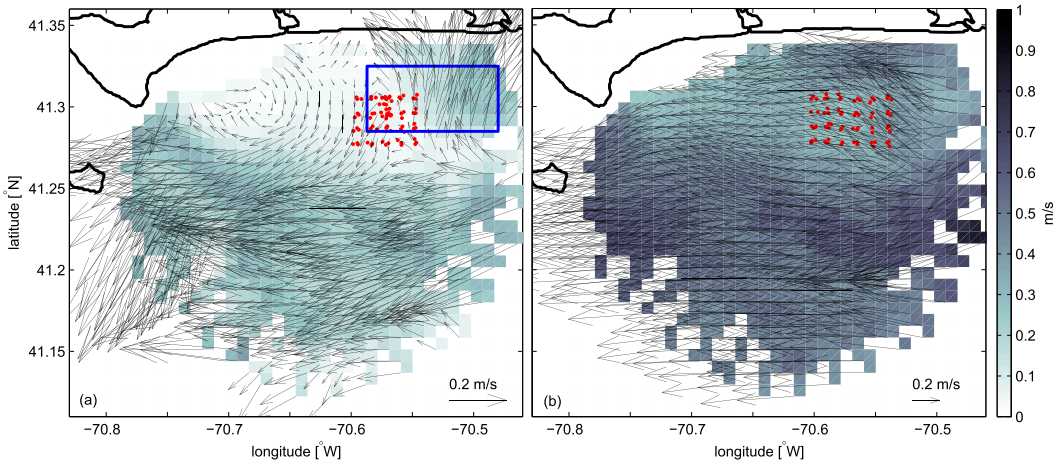

FIG. 1. Snapshots of the HF radar-based surface velocity fields south of Martha's Vineyard, Massachusetts, at the end of drifter release for the (a) August and (b) September 2014 field experiments. Drifter deployment positions are shown in red. Blue rectangle shows the domain where the dye measurements were made (same domain as in Fig. 5).

unresolved scales of motion when modeling the spread of a tracer in the ocean.

Thus, this work investigates the validity and limitations of the drifter-based diffusivity estimates in realistic oceanic settings. The 2014 field experiment south of Martha's Vineyard, Massachusetts, is described in section 2, while section 3 discusses our findings and places them into context with earlier diffusivity studies. Key conclusions are summarized in section 4.

2. 2014 field experiment in the coastal ocean south of Martha's Vineyard, Massachusetts

Three essential components are required to investigate and test the concept of eddy diffusivity in real oceanic settings: 1) an observing system or numerical model into which the unresolved and underresolved motions can be added through the eddy–diffusion-based parameterization, 2) observational data for estimating eddy diffusivity values, for example, from Lagrangian instruments, and 3) an independent observational dataset for evaluating the performance of the eddy diffusivity approach. An opportunity to obtain all three essential components was provided by a comprehensive observational field program aimed at understanding the exchange and dispersion processes across the inner shelf south of the island of Martha's Vineyard, Massachusetts. As part of this field program in summer–fall 2014, simultaneous release of dye and near-surface drifters was carried out within the footprint of a high-resolution HF radar system.

a. *General physical oceanographic description of the inner shelf south of Martha's Vineyard*

The largest current variability over the inner shelf south of Martha's Vineyard in summer is due to the tides. Tidal currents in this region are strong with large spatial variations. The amplitude of tidal currents associated with the M_2 tidal constituent varies from 60 cm s^{-1} in the east near Muskeget Channel, decreasing to 15 cm s^{-1} in the middle of the domain and increasing again to 30 cm s^{-1} at the western edge of the domain (Fig. 1). In summer, there is a mean westward surface current jet with a maximum of 15 cm s^{-1} roughly 15 km offshore. The mean westward current decreases to near 0 cm s^{-1} within about 5 km of the coast. There is also a tidally rectified, semipermanent anticyclonic recirculation in the northeastern portion of the domain. Standard deviations of summer detided currents range from 10 cm s^{-1} near the coast to ~15 cm s^{-1} in the vicinity of the offshore jet.

Previous work by Kirincich (2016) has examined the occurrence, drivers, and implications of small-scale O(2–5) km diameter coherent vortices over the inner shelf south of Martha's Vineyard, Massachusetts. Coherent vortices or eddies were found to occur at rates of 1 and 4 day^{-1} in winter and summer, respectively. Most were less than 5 h in duration, smaller than 4 km in diameter, and rotated less than once over their lifespan; 60% of the eddies formed along the eastern edge of study area, adjacent to Wasque Shoal, and moved westward along the southern coast of Martha's Vineyard, often with relative vorticity greater than the Coriolis parameter f. Eddy generation was linked to

vortex stretching on the ebb and flood tide as well as the interaction of the spatially variable tide and the wind-driven currents. Eddies located away from Wasque Shoal were related to the movement of wind-driven surface currents, as wind direction controlled where eddies formed as well as density effects.

b. The Martha's Vineyard HF radar system

The high-resolution HF radar system was composed of three sites with SeaSonde-type direction-finding instruments running at operating frequencies of about 25 MHz. The three sites were located approximately 10 km apart along the southern coast of Martha's Vineyard, Massachusetts, and measured surface currents within roughly a 30 km × 30 km domain south of the island. Raw radials from the three radar sites were converted into snapshots of 2D near-surface velocities at a nominal resolution of about 800 m at fully independent half-hour time intervals (Kirincich et al. 2012, 2013). Because of the use of azimuthal bins, however, the actual resolution of the velocity field varies slightly throughout the domain. Two sample radar-based velocity snapshots corresponding to the times of drifter deployments for the August and September 2014 field experiments (described in the next subsection) are shown in Fig. 1. The effective depth of the velocity estimates obtained by the 25-MHz radar system is about 0.5 m (Stewart and Joy 1974). Comparisons to in situ, ADCP-based, near-surface (3–4-m depth depending on location) velocities made at eight locations within the radar domain during 2014 suggest the radar system was performing optimally, with RMS differences of 4–10 cm s^{-1}. Output from the same HF radar system has been recently analyzed in detail in Rypina et al. (2014), although for a slightly different geometrical configuration of the three antenna sites. In that work the radar-based predictions of surface drifter trajectories were found to have minimal biases, with errors mainly related to the spatial averaging inherent to the radar sampling. Specifically, the radar accuracy, quantified by the domain-averaged RMS difference between instantaneous radar and drifter velocities, was found to be about 3.8 cm s^{-1}, while the separation speed between the real and radar-simulated drifter pairs deployed at the same time and location was about 2.8 cm s^{-1}, leading to separation distances of 1 km after 10 h.

c. Mass drifter releases in August and September 2014

In August 2014, 75 Coastal Ocean Dynamics Experiment (CODE)–type near-surface drifters were released south of Martha's Vineyard, Massachusetts, in a 4 km × 3 km domain lying within a footprint of the Martha's Vineyard HF radar system described above. The 60 drifters were deployed in triplets with approximately 100-, 200-, and 225-m spacing between drifters in each triplet and 1-km spacing between the neighboring triplets. The remaining 15 drifters were deployed at regular arclength intervals along a spiraling dye release pattern that is described in the next subsection. Drifters were deployed from two coastal vessels over a time span of 2.5 h and generally left in the water for 3 days (four drifters were left in the water for additional 1–4 days). Recovery was facilitated by a fully autonomous software package developed by the authors (Rypina et al. 2014). The software informs each vessel, in real time, of the location of the nearest drifters to it within an assigned recovery area, streamlining the recovery process such that 70 drifters (spanning an area over 2000 km^2) were successfully recovered within a 1-day, two-vessel field operation. Drifter's GPS positions were logged at 10-min intervals and transmitted onshore via Iridium-based text messaging. The GPS positioning error is ~3 m according to the manufacturer and based on tests done at Woods Hole. Drifters were manufactured by MetOcean based on the technical specifications of the original CODE drifter developed by Dr. Russ Davis of Scripps Institution of Oceanography (SIO) and thus had similar water-following capabilities. Drifters of the same design have been recently used by Rypina et al. (2014) and C. Chen et al. (2014) as well as being the standard design used by the U.S. Coast Guard for their search and rescue operations. Recent estimates of the expected slip of CODE-type drifters with standard sails spanning the top 1 m of the water column are 1–2 cm s^{-1} during light wind conditions typical of the summer south of Martha's Vineyard (Ohlmann et al. 2007; Poulain et al. 2009). During stronger winds, published slippage estimates are more variable but generally increase to 1–3 cm s^{-1} (Molcard et al. 2009; Poulain et al. 2009).

Drifter trajectories from the August 2014 field experiment are shown in Fig. 2a from the time of their release until they exited the HF radar domain. Most of the drifters left the domain through the northeastern boundary going eastward toward Wasque shoals (a shallow area south of the southeastern tip of the island) and headed into the narrow Muskeget Channel located east of the island. The flow over the shoals and in the channel is strongly tidally dominated, and as a result some of the drifters reentered the HF radar domain as the flow reversed direction on the next ebb tide. A smaller group of drifters, originating from the southwesternmost deployment locations, turned to the southwest and continued moving in that direction with a few loops, cusps, and wiggles until the drifters left the HF radar domain 1.5–2 days later.

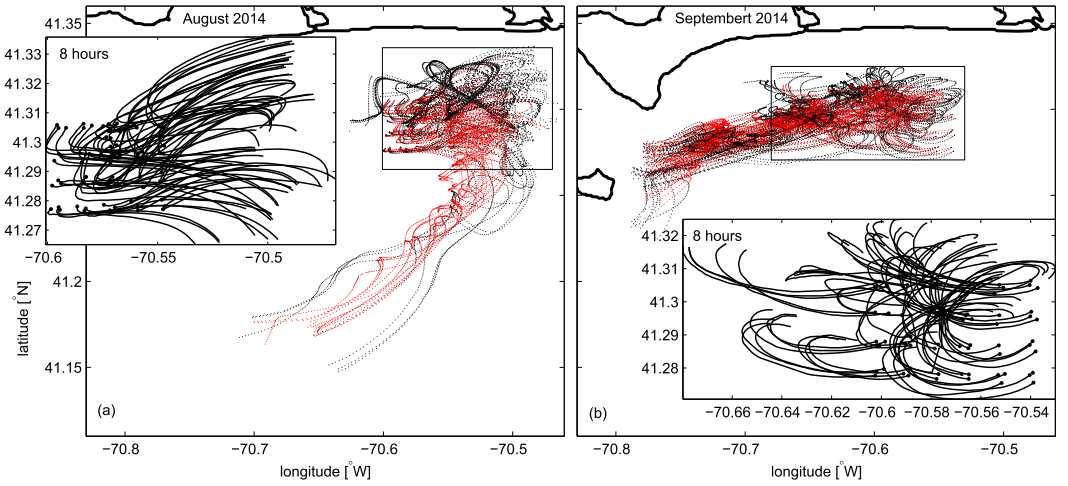

FIG. 2. Real (black) and radar-based simulated (red) trajectories for the (a) August and (b) September drifter release experiments. Segments of trajectories are shown from the time and location of drifter deployment until they leave the radar domain. On average, drifters stayed in the radar domain for approximately 20 (36) h in August (September). Insets show the initial 8-h-long segments of drifter trajectories for the August/September releases.

The second drifter deployment and recovery was carried out 1 month later in September 2014; 24 triplets (=72 drifters) with the same spacing between drifters as in August were deployed within a 5 km × 3 km domain centered at the August grid but extending an extra 0.5 km to the west and east. Drifters were left in the water for 3 days, again logging and transmitting their positions every 10 min, and recovered afterward. The main difference between the two deployments was the weather conditions. The first day of the September deployment coincided with the onset of strong winds to the west, leading to remarkably different drifter trajectory patterns (Fig. 2b) compared to the August experiment (Fig. 2a). In September, after some initial looping motion, all drifters moved westward across the HF radar domain, with most drifters leaving the domain through the western boundary 1.5 days later. A few of the northernmost drifters entered the area to the east of Squibnocket Point (the southernmost corner of the island) that is not covered by the radar due to the geometry of the HF radar sites.

d. Dye release experiment

The dye was released, contemporaneously with the August 2014 deployment of drifters, along an outward 4-km-long spiral centered about 4.5 km south of Martha's Vineyard and reaching approximately 800 m in diameter by the end of the outer leg of the spiral. The spiral was located within the footprint of the HF radar and was spanned by the 20 drifter triplets. Additionally, 15 drifters were released in the dye streak during the dye release at equal arclength intervals along the spiral. The dye mixture of Rhodamine (Rhd) WT, Fluorescein, and isopropyl alcohol was premixed onshore to match the density of the seawater at 0.5–1 m below the surface, which coincided with the effective depth of the CODE drifters. The resulting dye solution was then further mixed with seawater to bring the total volume to 180 L. The dye mixture was pumped into the ocean at a constant rate of 6 L min^{-1} along the spiral in just under 30 min at a ship speed of ~6.5 kt (1 kt = 0.51 m s^{-1}). The prepared dye mixture contained a total of 4.8 kg of Rhd, was dark orange/brown in color, and was clearly visible from the vessel during the deployment and an hour or so afterward, simplifying the dye release and survey operations. Aerial photographs of the dye mixture in the ocean were also taken during the dye release from a remotely controlled (from the ship) airborne quadcopter equipped with a digital camera (Fig. 3).

After completion of the dye release, an intensive ship-based survey of the dye was carried out. A WET Labs fluorometer tuned to the frequency of the Rhodamine dye was incorporated into the R/V *Tioga*'s flowthrough system, providing real-time information on dye concentration at the depth of *Tioga*'s water intake, approximately 1 m. This fluorometer provided Rhd readings every 2 s, thus allowing for spatially dense surveys even at relatively high ship speeds. A second fluorometer tuned to the frequency of Rhd, a Chelsea Aquatracka, operated as part of a towed, undulating SeaBird 19 CTD system (the Guildline MiniBAT). Both fluorometers were laboratory-calibrated prior to the field experiment for the potential range of Rhd concentrations observed in the field, allowing for a precise

FIG. 3. Georectified aerial image of the dye taken by the quadcopter-mounted camera on 1050 EST 4 August 2014, 23 min after the beginning of the August 2014 dye release experiment. The dye spot in the southwest corner belongs to the initial segment of the spiral release pattern; however, the exact starting point is slightly outside of the image bounds. The R/V *Tioga* is shown at right; the length and width of the vessel are 18.3 and 5.2 m, respectively. Point A marks the position used to estimate the image-based diffusivity, with arrows indicating the width of the dye streak at point A and behind the ship.

conversion from raw voltage measurements into the Rhd concentrations in parts per billion. The MiniBAT system also provided real-time visualization of the data, via a conducting cable, and was towed from the ship in an undulating fashion spanning approximately the top 10–12 m of the water column. Each down- and upcast (i.e., each sawtooth) took about 60 s, leading to approximately 180-m separation between same depth measurements from neighboring casts at a ship speed of 6 kt. The depth-profiling measurements from the MiniBAT system augmented the Rhd concentration estimates collected via the flowthrough system allowing for monitoring of the dye concentrations and rapid decision-making during the dye surveys. Survey patterns were zigzags, guided by the movement of the drifters (also monitored in real time) and adjusted based on observations from the flowthrough and MiniBAT fluorometers.

Because of the time restrictions on ship-based operations, the slower MiniBAT system was only operated for about an hour following the dye release, providing 42 clean upcasts with the vertical span from approximately 1 to 11 m below the surface (Fig. 4). After recovery of the MiniBAT, surveys continued for 7.5 h after the dye release using the flowthrough fluorometers, which could be operated at faster ship speeds. The Rhd concentrations (ppb) measured by the flowthrough fluorometers during the first 2 h of the postdye deployment survey suggest that for a few hours after the release, the center of mass of the dye stayed in the same geographical area as the release spiral (Fig. 4). We will refer to this initial part of the survey as the "near-field" pattern. Consistent

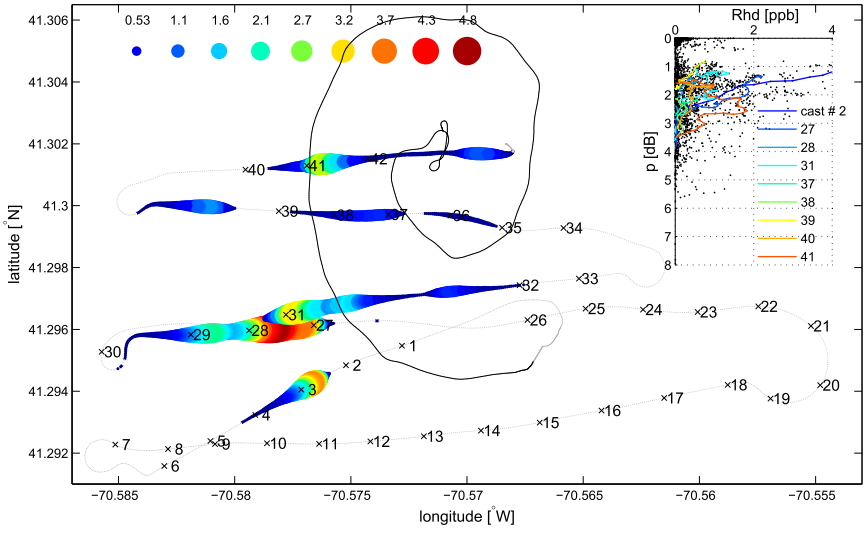

FIG. 4. Segment of R/V *Tioga*'s ship track from start of the dye release at the center of the spiral until the end of the dye release (black spiral) and from start to end of the MiniBAT survey (gray curve). Rhd concentrations (ppb) from the flowthrough system are shown in color. Geographical locations of the start (i.e., bottom point) of each clean MiniBAT upcast are shown by black crosses with the number of the cast marked next to each cross. (small inset) Vertical distribution of Rhd in the top 10 m of the water column from the MiniBAT survey. All data points are shown in black; data from clean individual upcasts, corresponding to the black crosses, are shown in color.

with the flowthrough fluorometer measurements, the MiniBAT fluorometer showed elevated Rhd values at 10 casts that were geographically coincident with the locations of the colored circles in Fig. 4. The vertical profiles from the MiniBAT indicated that, at least during the first hour after release, the dye stayed within the top 5 m of the water column. This estimate is consistent with typical values of the mixed layer depths during summer low-to-moderate wind conditions. Interestingly, while observations made right after the dye release seemed to indicate surface-intensified Rhd concentration profiles, observations made about an hour later, specifically cast 41, suggested the presence of a subsurface Rhd maximum located at ~2.5 m. Unfortunately, no estimates of the vertical distribution of Rhd are available in the far field.

A few hours after its release, the dye patch started to move eastward. By 7.5–8 h it had moved ~10 km from its release location (Fig. 5a). This part of the survey will be referred to as the "far field." As the dye moved eastward along the shoreline of Martha's Vineyard, it started to disperse, leading to an approximately tenfold decrease in Rhd concentration compared to the highest near-field values. In the far field, the ship track intersected the dye plume four times, producing four elevated "hot spots" of dye along the survey track located near 70.52°E, 70.51°E, and 70.505°E and the smallest easternmost hotspot near 70.49°E (Fig. 5a).

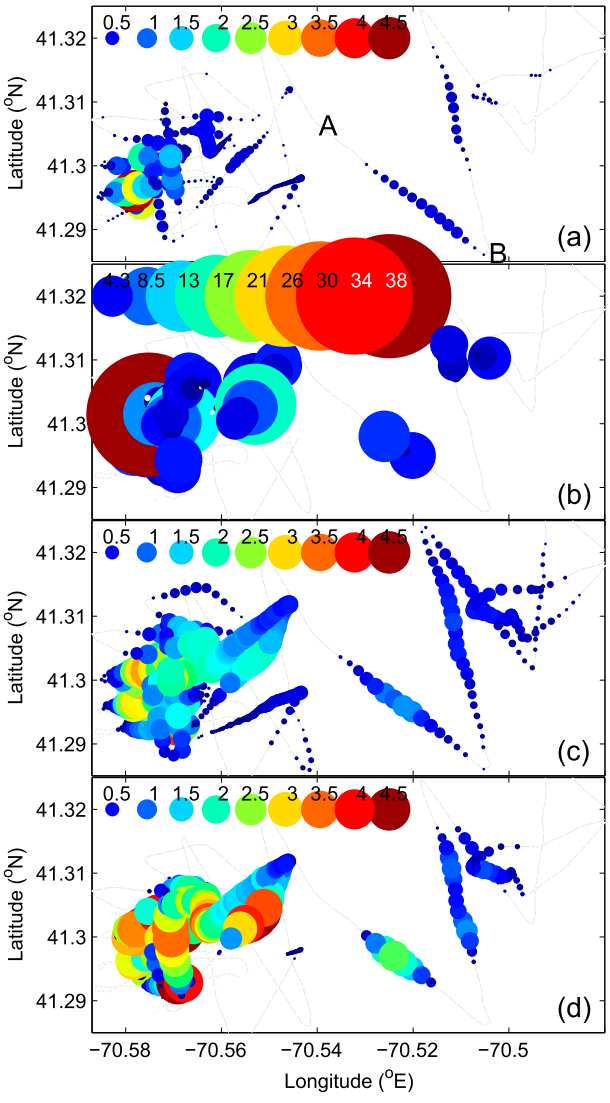

FIG. 5. Rhd concentrations along the ship track (a) measured, simulated using radar velocities (b) without diffusion, (c) with drifter-based diffusion, and (d) with Okubo diffusion. Rhd concentrations (ppb) are shown both by color and size of circles, with large red indicating largest concentrations, small blue indicating the smallest, and gray dots indicating zero. For reference, 0.01° latitude/longitude is 1.1/0.8 km. Survey duration is 8 h. A and B in (a) mark the transect that is referred to in text.

3. Testing the eddy diffusivity concept using data from the 2014 field experiment

A contemporaneous dye and drifter release within the footprint of a high-resolution HF radar system provides a unique opportunity to test and quantify the performance of the eddy diffusivity concept in the coastal ocean. The idea behind the test is simple: the HF-based surface currents can be combined with the drifter-based diffusivity representing the effects of the unresolved and underresolved scales to mimic the evolution of the dye patch in the ocean. The simulated dye concentrations can then be sampled in the same manner as was done during the field experiment, and the resulting simulated Rhd concentrations along the ship track can be compared with measured dye concentrations to evaluate the performance of the scale-dependent, model-specific eddy diffusivity approach. An implicit assumption behind augmenting radar measurements with drifter-based eddy diffusivity is that differences between the radar and drifter measurements are due to small-scale motions and thus are well represented by the diffusive process. If the two types of measurements are widely inconsistent with each other in reproducing flow components other than small scale, it would be unphysical to use diffusion to parameterize the differences between the two. Before proceeding, it is thus worth comparing the HF radar measurements with drifters.

a. *Eulerian and Lagrangian correspondence between the HF radar and drifters*

The sequential 10-min GPS position fixes for each drifter can be converted into estimates of the local

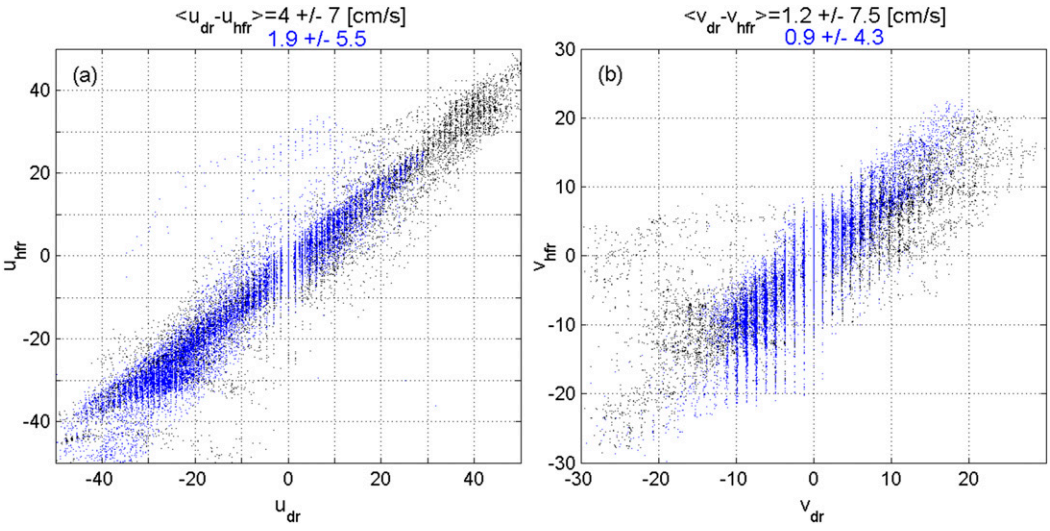

FIG. 6. Scatterplots of the HF radar-based (denoted by subscript "hfr") vs drifter-based (denoted by subscript "dr") velocity components (cm s^{-1}) in the (a) zonal and (b) meridional directions for the August (black) and September (blue) experiments. The mean and std dev values are shown above each subplot.

velocity. On average, buoys drifted approximately 130 (120) m in 10 min during the August (September) experiment, corresponding to an average speed of approximately 22 (20) cm s^{-1}. These drifter-based velocity estimates were compared to radar-based velocities interpolated to the times and locations of the drifters. We used bilinear interpolation in space and time to interpolate radar velocities; however, the results are insensitive to the interpolation technique used and we only list the details here for completeness of the discussion. Specifically, the mean and standard deviation (std dev) of the differences between the radar and drifter velocities change by 10% or less if we use the closest point approach instead of bilinear interpolation. For the August drifter release, scatterplots of the radar versus drifter velocities for zonal (u) and meridional (v) components are presented in Fig. 6. The mean and std dev values of the difference between the radar and drifter velocities were 4 ± 7 and 1.2 ± 7.5 cm s^{-1} for u and v, respectively. These values include the contribution from drifter's wind slippage and non-Lagrangian effects. The September data (also Fig. 6) were generally comparable, although slightly better, with Eulerian correspondence between radar and drifter velocities of 1.9 ± 5.5 and 1 ± 4.3 cm s^{-1} for u and v, respectively. This similarity between the August and September results suggests that the relative uncertainty of the radar does not vary significantly between the weak (August) versus moderate-to-strong (September) wind conditions. The vertical stripes seen in the scatterplots at small values of the drifter velocities are due to the GPS positioning data being limited to the fifth significant digit in the measurements of the latitude and longitude. Outlier points in Fig. 6, where the difference between radar and drifter velocity estimates exceeds 3 STDs, come from the geographical area near 41.3°N and 70.5°E, which lies close to the edge of the radar domain (see Fig. 1) where its performance deteriorates. This area is also characterized by the diverging trajectory pattern in Fig. 2a, perhaps indicating elevated sensitivity to initial positions in this region. Overall, Fig. 6 suggests that drifter- and radar-based velocities agree reasonably well with each other, especially considering the various potential causes for the mismatch, including the GPS positioning error, differences in effective depths of the two instruments (0.5 m for radar and 1 m for drifters), drifter wind slippage (1–3 cm s^{-1}), as well as smoothing, time averaging, and interpolation associated with the processing of the raw radar radials from each antenna site into half-hourly snapshots of uniformly gridded velocity fields.

Gridded maps of radar velocities can also be used to simulate the motion of drifters as they are advected by the oceanic flow. The resulting simulated trajectories (red curves in Fig. 2) can then be compared to the real drifter trajectories (black curves in Fig. 2) in order to quantify the Lagrangian correspondence between the two. We used a variable-step fourth-order Runge–Kutta trajectory integration scheme [RK4(5) in MATLAB] with bilinear velocity interpolation in space and time to compute the simulated trajectories, but again our results are insensitive to the integration and interpolation routines used. Overall, the distribution of simulated trajectories agrees well with that for the real drifters in

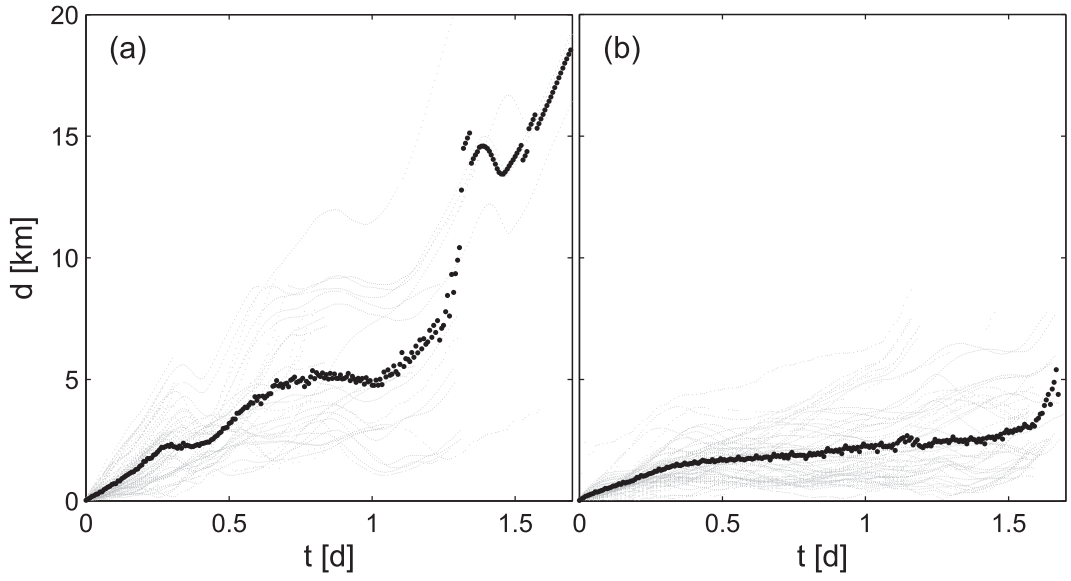

FIG. 7. Separation between the real and simulated (using the HF radar velocities) drifter pairs released at same time and location for the (a) August and (b) September experiments. Trajectories are terminated when either real or simulated drifters leave the radar domain. Gray shows individual pair separations; black shows the mean averaged over all pairs.

terms of the general shape and extent of the trajectory cloud, however, the small-scale details of individual trajectories such as the exact positions, shapes, and sizes of wiggles, loops, and cusps differ between the two. As a result, real and simulated drifters initially released at the same time and location diverge from each other, and the resulting separation (Fig. 7) can be used to quantify the ability of the HF radar system to reproduce the Lagrangian data. For the August drifter release, the real and simulated drifters separated by roughly 5 km in 1 day. At longer times, most drifters left the radar domain, and the remaining large separation values are dominated by a small group of trajectories that, unlike the rest of the drifters, moved southwestward across the domain. This cluster is clearly visible in both real and simulated trajectory distributions, and in both cases these trajectories originated from the southwestern corner of the deployment grid. However, the exact release location of those trajectories that go to the southwest differs slightly between the real and simulated datasets. Thus, in these locations, potentially small differences between the initial radar and drifter fields led to large separations between the resulting real and simulated trajectories (20 km) after 2 days. As a result, separation values at times longer than about a day are probably biased high and not representative of the general trend. In September, the separations between real and simulated trajectory pairs were generally smaller, reaching only about 2 km after 1 day. This is likely a consequence of the strong wind conditions, which gave rise to strong along-shelf westward velocities (Fig. 1b) that caused drifters to stay closer together and move westward across the HF radar domain as a single group instead of separating into different clusters (Fig. 2b). The smaller Lagrangian separation is also generally consistent with the slightly better Eulerian agreement for the September data compared to the August data. The Lagrangian separation values for September were consistent with separation estimates of 1 km in 12 h reported by Rypina et al. (2014).

To summarize, the radar and drifter datasets are in general agreement, with slight mismatch due mostly to the inability of the radar to resolve small scales of motion. This justifies the use of drifter-based diffusivity to parameterize small-scale motions that are unresolved or underresolved by the radar. Since drifters were advected by the full flow, which included all scales of motion, whereas radar data are limited to the prescribed spatiotemporal resolution, the combination of the two can be used to estimate small-scale eddy diffusivity using the pseudotrajectory approach described in section 1c. However, it is important to keep in mind that drifters, and thus drifter-based diffusivities, have their own set of limitations associated with GPS accuracy, wind slippage, limitation to stay at the surface, and so on. Nevertheless, as we show below, simulations that included drifter-based diffusivities resulted in more realistic dye distributions compared to those where dye was advected by

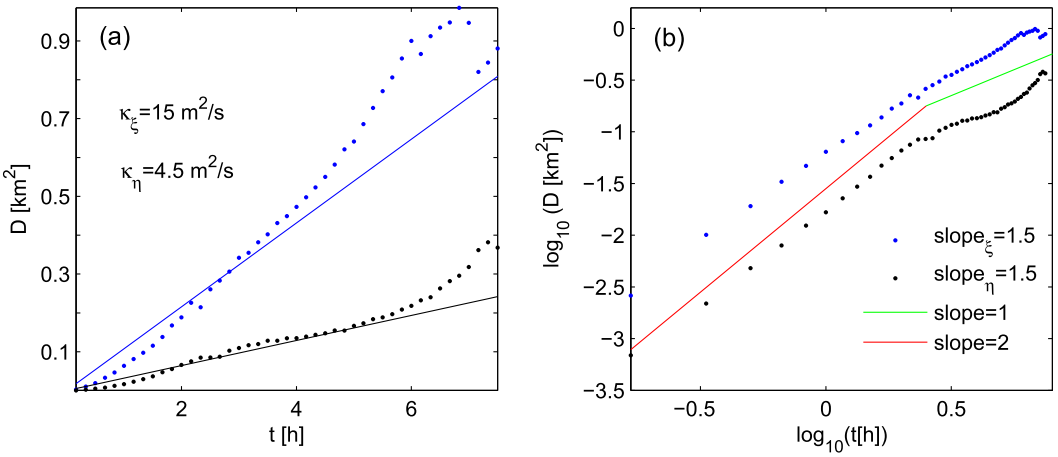

FIG. 8. Radar-specific single-particle dispersion, D_ξ (blue dotted) and D_η (black dotted), computed using pseudotrajectory method via Eqs. (4), (1), and (2) as a function of time on (a) linear and (b) logarithmic scales for the August experiment. The numbers in (a) show diffusivities in the direction of the fastest spreading (65° with respect to a zonal direction) and in the perpendicular direction. Black and blue lines show mean slopes for dispersion curves in the direction of the fastest spreading and perpendicular direction, respectively. Red/green lines in (b) show ballistic/diffusive regimes; transition between red and green was arbitrarily chosen to visualize concepts described in text.

radar velocities alone or in combination with the widely used Okubo diffusivity estimate.

b. *Scale-dependent, radar-specific, drifter-based diffusivity*

We now proceed to apply ideas presented in section 1c to the drifter and radar data. Specifically, we used Eqs. (4), (1), and (2) to estimate the eddy diffusivity that is specific to the Martha's Vineyard HF radar and that represents the effects of small-scale motions that are unresolved or underresolved by this particular radar system (800-m resolution). At each 10-min time interval following each real drifter trajectory, we subtracted the displacement predicted by the radar from the real displacement of the drifter and then summed up the residual displacements according to Eq. (4) to form pseudotrajectories. These pseudotrajectories were then used to estimate the components of the dispersion tensor according to Eq. (1) as a function of time (Fig. 8). We then computed the mean slope of the resulting D versus t curve by taking a time average of $D(t)/t$ over 8 h and used Eq. (2) to obtain the small-scale eddy diffusivity to be used in combination with this particular radar system for numerically simulating the spreading of the dye during the August 2014 field experiment. Note that the mean slope computed as described above is slightly smaller than that for a least-squared linear fit, which is not constrained to go through the origin. The obtained diffusivity values are $K_\xi = 15\,\mathrm{m^2\,s^{-1}}$ and $K_\eta = 4.5\,\mathrm{m^2\,s^{-1}}$, with the corresponding mean angle of maximum spreading $\theta = 65°$ with respect to the zonal direction. Generally, it is not well understood what sets the direction of the fastest spreading for pseudotrajectories. Rypina et al. (2012), for example, found that in the North Atlantic the major axis of the diffusivity ellipse is aligned with the direction of the mean flow in parts of the domain such as near the Gulf Stream but is perpendicular to the mean flow at other locations such as in the eastern subtropical gyre. In addition, the direction of the fastest spreading may also be scale dependent. Because the ship-based surveys had mapped out the dye distribution for up to 8 h after the dye release, we restricted our attention to those time scales only and used the initial 8-h segments of the trajectories to estimate eddy diffusivity. Note that even after 8 h, the spread of the pseudotrajectories was just less than 1 km, which is only slightly more than the 800-m resolution of the HF radar system's grid spacing. Also, diffusivities in this study were assumed to be spatially homogeneous. This simplification is motivated by the assumption that the eddy-induced motions that we aim to parameterize do not exhibit strong spatial dependence over the scales considered here. Note also that our drifter dataset, although quite rich, is still not large enough to allow reliably estimating the spatial variability of the eddy diffusivities. For these reasons, a more thorough investigation of the spatial structure of diffusivities is left for a future study.

Drifter-based dispersion curves for both $D_\xi(t)$ and $D_\eta(t)$ on a logarithmic scale are shown in Fig. 8b. Consistent with the general expectation that the spreading becomes diffusive only after some initial adjustment

time, the drifter-based dispersion curves indicate that ballistic growth dominates at very small times, with a transition to a slower and more diffusivelike spreading several hours later. The deviation from, and late onset of, diffusive regime are also consistent with the fact that over 8 h drifter trajectories barely sample several submesoscale eddies, whose typical length scale in this area is a few kilometers according to the recent analysis by Kirincich (2016). Note, however, that the dispersion curves in Fig. 8 characterize the spreading of the pseudotrajectories (rather than real trajectories) caused by the small-scale component of the velocity field that is unresolved or underresolved by the radar (rather than by the full velocity field), which roughly corresponds to length scales smaller than about 1 km. The larger-scale shear, which is a major contributor to a ballistic spreading of real drifters, will at least partially be explicitly resolved by the radar and thus is expected to contribute less to the dispersion of pseudotrajectories. As a result, one might expect that a transition to a diffusive regime would start sooner for the pseudotrajectories than for the real trajectories. The exact timing of the onset of diffusion is challenging to predict for the pseudotrajectories and might be difficult to interpret in terms of the dominant eddy scales. The overall slope of the best-fit line to the drifter-based dispersions $D_\xi(t)$ and $D_\eta(t)$ on a logarithmic scale is about 1.5, which further suggests that the spread of the pseudotrajectories was somewhere between ballistic and diffusive regimes during the initial 8-h time period. Finally, note that the eddy diffusivity approach for parameterizing unresolved scales of motion ignores the fact that the real underlying dispersion process is not quite diffusive but simply fits a ''best-fit diffusive process'' that gives a comparable spread of particles or drifters to that observed over the same time interval.

c. *Simulating the dye distribution using HF radar field with and without drifter-based eddy diffusivity*

The evolution of dye in the ocean was simulated numerically using a Lagrangian approach, where we released a large number of (infinitesimally) small water parcels along the spiral dye release pattern taken from the real field experiment and assigned a fixed mass of Rhd to each water parcel such that the integral over all parcels was normalized to give the total released amount of Rhd (4.8 kg). These simulated particles were then advected using the radar-based velocity field with and without an additional stochastic velocity component whose parameters were fitted to match a prescribed value of the radar-specific, drifter-based, small-scale eddy diffusivity tensor, that is, the K_ξ, K_η, and θ estimates from section 3b. Because dye was released into water behind R/V *Tioga*, the initial dye streak width was at least as large as *Tioga*'s beam (5.2 m) but probably larger due to the effect of the ship's wake. To account for this effect, in our numerical simulations, we released dye-carrying water parcels within a 40-m square centered at the (moving) ship location. Simulations with the added diffusion are not sensitive to the initial streak width because the diffusive spreading of the dye will quickly overcome any reasonable value of the initial streak width. Decreasing initial streak width in simulations without diffusion, however, would result in narrower, more compact and more concentrated dye distributions, thus leading to poor agreement with observations. To simulate the diffusive process, at each time interval $dt = 30$ s, following each water parcel trajectory we superimposed an additional stochastic velocity $\mathbf{u}_{\rm diff}$ onto the local radar-based velocity $\mathbf{u}_{\rm radar}$. The zonal and meridional components of the stochastic addition were $u_{\rm diff} = u_{\rm rand}\cos\theta - v_{\rm rand}\sin\theta$ and $v_{\rm diff} = v_{\rm rand}\sin\theta + u_{\rm rand}\sin\theta$, where $u_{\rm rand}$ and $v_{\rm rand}$ were normally distributed random variables with zero mean and std dev $u_{\rm std} \propto \sqrt{K_\xi/dt}$ and $v_{\rm std} \propto \sqrt{K_\eta/dt}$. Here, a proportionality coefficient of ~2.6 was chosen empirically via an iterative method to match the diffusivity values for the distribution of stochastically moving particles resulting from such random walk process to the observed K_ξ, K_η, and θ after 8 h. To estimate the distribution of dye at some time t after release, the distribution of simulated water parcels at that time was binned into square 100-m bins, the mass of Rhd (kg) in each bin was estimated by summing over all parcels in the bin, and the concentration of Rhd (ppb) in each bin was then computed by dividing the mass within each bin by the bin volume $V_{\rm bin} = x_{\rm bin}y_{\rm bin}z_{\rm mld}$, where the depth of the bin was taken to be equal to the mixed layer depth: $z_{\rm mld} \approx 5$ m. In other words, the calculation assumes that dye is equally distributed in the vertical over the 5-m-deep mixed layer, which is a reasonable first approximation based on the measured vertical profiles of Rhd shown in Fig. 4.

In our Lagrangian approach, where a fixed amount of Rhd is assigned to many infinitesimal fluid parcels at the source location and the resulting amount of dye at each geographical location at a later time is constructed by summing over all parcels in the corresponding bin, using larger bins is equivalent to spatially averaging the dye field constructed using smaller bins. The bin size of 100 m used in our numerical simulations was chosen as a compromise between the accuracy of numerical simulations (smaller bins require more Lagrangian particles to be released) and the ability to resolve small-scale features in the resulting dye distribution (using larger bins will remove small-scale variability). Because the length scale of the individual hot spots, as measured by

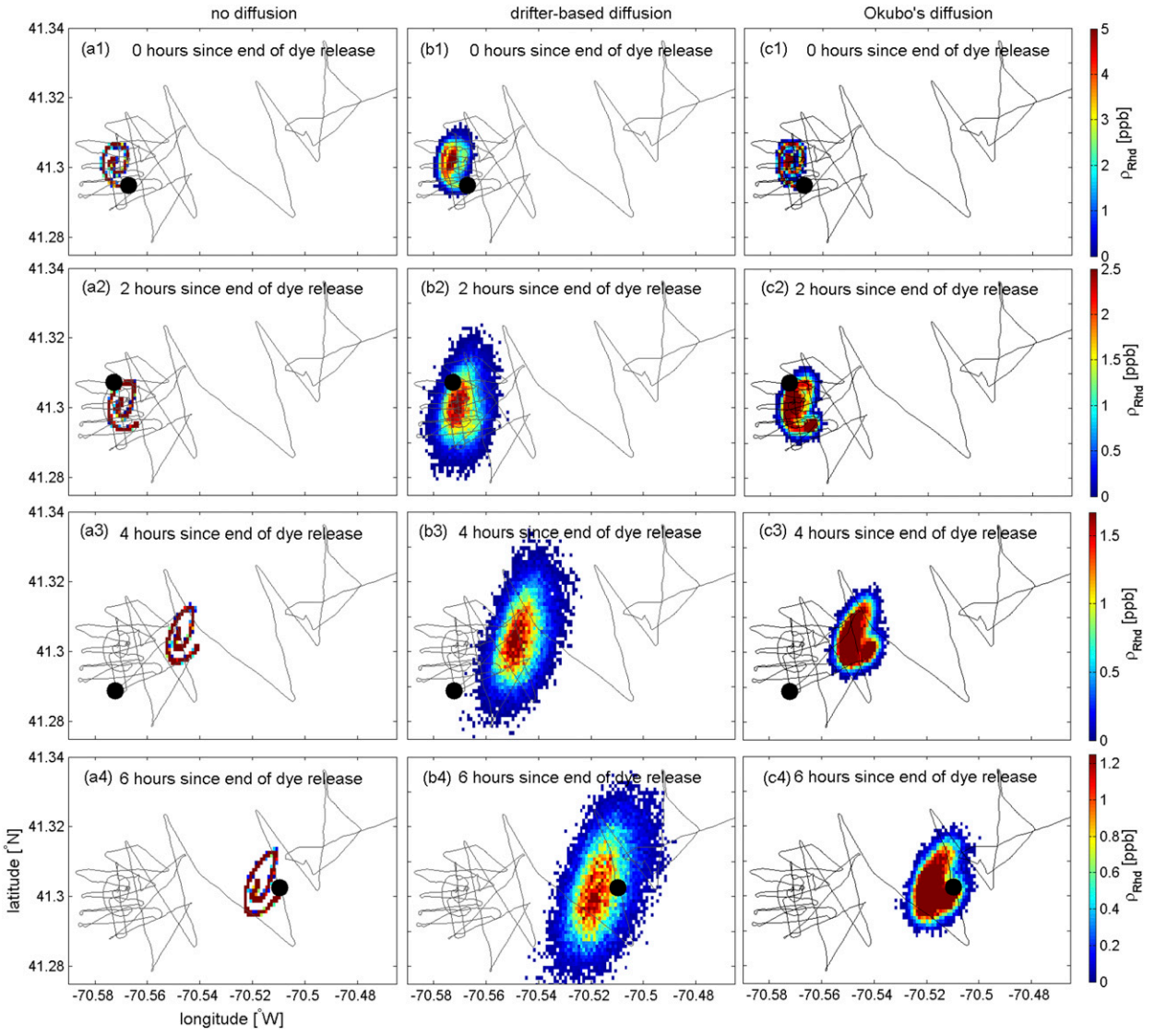

FIG. 9. (a1)–(a4) Predicted radar-based dye distributions at 0, 2, 4, and 6 h since the end of the dye release in simulations without diffusion, (b1)–(b4) with anisotropic drifter-based diffusion and (c1)–(c4) with isotropic Okubo diffusion. Ship track is shown in black, with the large black dot indicating the contemporaneous position of the ship.

the shipboard, flowthrough Rhd measurements, was on the order of a few kilometers or less, the bin size required to resolve this variability is $O(100)$ m. Finally, to minimize the effect of bin size on the comparison between observations and simulations in Fig. 5, flowthrough Rhd concentrations in Fig. 5c were low-pass filtered with a 100-m length scale equal to the bin size in our simulations. Note, however, that along-track smoothing of the flowthrough data differs from the 2D spatial averaging, so the dependence of the simulations-to-observations comparison on the bin size is minimized but not completely eliminated by performing the described spatial averaging.

Radar-based predictions for the dye distributions at 0, 2, 4, and 6 h since release are shown in Fig. 9 for the case without [Figs. 9a(1)–9a(4)] and with [Figs. 9b(1)–9b(4)] drifter-based diffusivity. The movement of the center of mass of dye is independent of diffusion and thus is the same between the corresponding Figs. 9a and 9b. In both cases, the dye patch moves eastward, stretching to the northwest and southeast and deforming from a circular spiral into an elongated elliptical shape. Without diffusion, the individual legs of the spiral are still clearly visible after 6 h. With diffusion, on the other hand, individual coils merge together after a few hours, producing a well-blended Gaussian elliptical patch. This

seems to be qualitatively consistent with the measured Rhd concentration along the AB transect (marked in Fig. 5a) through the dye plume approximately 6 h after the end of dye release, which suggests that, although not completely homogenized into the Gaussian patch by that time, the dye distribution no longer shows pronounced individual peaks corresponding to different spiral coils. This is also consistent with the aerial images of the dye taken by the quadcopter-mounted photo camera, which shows that after 9 min neighboring spiral coils widened to almost half the initial distance between them (see Fig. 3), although it is possible that the initial widening of the dye streaks could be significantly enhanced by the effects of the ship's wake.

Finally, to compare simulated and observed dye distributions, we surveyed the simulated Rhd concentration fields in the same manner as was done during the field experiment, that is, we sampled the simulated distributions of dye at times and locations along the actual ship track. The resulting numerically simulated dye concentrations along the ship track are shown in Fig. 5 for the runs without (Fig. 5b) and with (Fig. 5c) the additional drifter-based eddy diffusivity superimposed on the radar velocity fields. Comparison between the observed dye distribution and the distribution resulting from the run without eddy diffusivity (Fig. 5a vs Fig. 5b) shows several important similarities as well as a few differences. The most striking difference is in the concentrations' values, which are an order of magnitude larger in the simulation without eddy-induced diffusion than in observations (>40 vs 4.8 ppb). Specifically, the simulated Rhd concentrations along the AB transect through the first hot spot are ~13 times higher than the observed ones. The details of the near-field distribution are not well represented in the simulation (Fig. 5b), which is perhaps not surprising since the intricate structure of the near-field depends on the details of the localized, small-scale flow features, which are not captured well by the radar. As suggested by Fig. 5c, these details are not parameterized well by the added eddy diffusivity either, as it accounts for the cumulative effect of eddies rather than for the effects of the individual eddy features. On the other hand, the general locations, but not magnitudes, of three out of four observed hot spots in the far field are represented fairly well in the simulation. Figure 5b shows pronounced isolated peaks in Rhd concentrations located near 70.52°E, 70.51°E, and 70.505°E on the three different zigzag legs of the survey. However, the smallest and weakest easternmost hot spot near 70.49°E, which is clearly visible in Fig. 5a, is missing in the simulation without eddy diffusivity. Finally, the simulated hot spots in Fig. 5b are overly localized, too compact, and too narrow compared to the wider and more diffuse peaks seen in the measured Rhd distribution in Fig. 5a. Thus, while the simulation without eddy diffusivity captured the general motion of the center of the dye patch fairly well, it failed to correctly reproduce the spreading of the dye patch and the decay of Rhd concentrations with time. This points toward the importance of small-scale features and clearly highlights the role of the unresolved and underresolved motions in shaping the dye distribution.

The simulated dye distribution resulting from the run with the radar-based advection and drifter-based eddy-induced diffusion is shown in Fig. 5c. As expected, the addition of the diffusive process led to a widening of the dye distribution and consequently to a decrease in dye concentrations. Both of these effects are clearly visible from comparing Fig. 5a versus Fig. 5c, and both act to bring the simulated dye distribution (Fig. 5c) closer to the observed one (Fig. 5a). Specifically, three main improvements are seen compared to the run without diffusivity. First, the simulated Rhd concentrations are now in a better agreement with the observations (Figs. 5a and 5c share the same color scale), with the simulated concentration values only slightly higher than the observed ones, instead of an order of magnitude higher as in Fig. 5b. Note that depending on the exact shape of the vertical distribution of Rhd, the assumption of the uniform vertical profile of the dye over the 5-m-deep mixed layer could lead to both larger and smaller concentrations compared to those at a fixed depth of 1 m below the surface, which corresponds to the depth of the water intake for the flowthrough system of R/V *Tioga*. However, since only a few measured vertical profiles of Rhd are available from the MiniBAT casts, all of them in the near field and some quite different from the others, we do not have enough information about the vertical structure of the dye distribution to move beyond the first-order assumption of the uniform vertical distribution. The second important improvement in the dye distribution concerns the fourth hot spot, the smallest and easternmost patch of dye located near 70.49°E, which has been reestablished in the dye distribution shown in Fig. 5c. Third, all four of the far-field hot spots have widened along the ship track substantially without shifting their location, improving the agreement with the observed Rhd concentrations in the top panel. Thus, all three aspects of the dye distribution discussed above, namely, the dye concentrations, the streak widths, and the number of hot spots along the ship track, agreed well with observations when we used the drifter-based diffusivity, giving us some confidence that this diffusivity tensor represents reasonably well the effects of the small-scale motions that were unresolved and underresolved by the radar. Larger diffusivity would lead to a

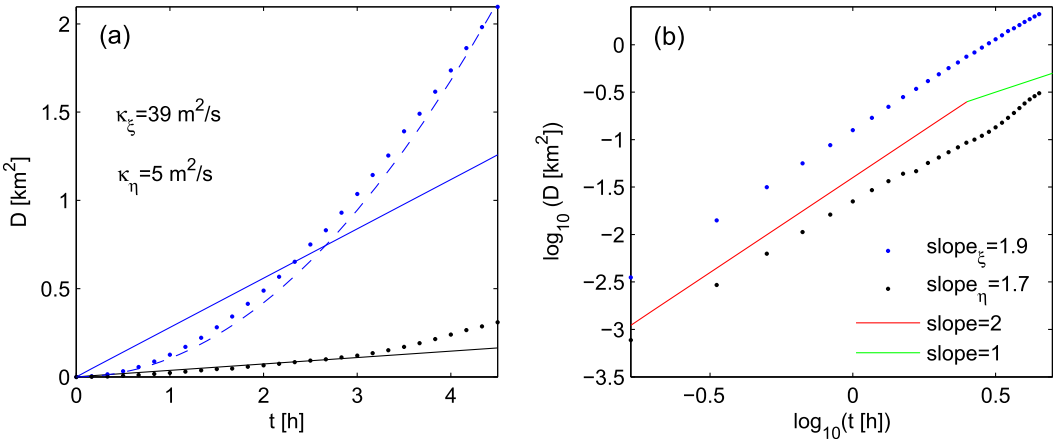

FIG. 10. Real drifter–based single-particle dispersion (blue and black dotted curves), computed using Eqs. (1) and (2), as a function of time on (a) linear and (b) logarithmic scales. The numbers in (a) show diffusivities in the direction of the fastest spreading (66° with respect to a zonal direction) and in the perpendicular direction. Blue dashed curve in (a) shows theoretically predicted ballistic spreading with velocity shear estimated from the radar velocities at time and location of drifter deployment. Blue and black solid lines in (a) show mean slopes for the dispersion curves in the direction of the fastest spreading and in the perpendicular direction, respectively. Red/green lines in (b) show ballistic/diffusive regimes.

wider and less concentrated dye distribution. Thus, if we increase the diffusivity values and keep the orientation and anisotropy (or aspect) ratio of the diffusivity tensor unchanged, the predicted dye distribution in Fig. 5c would be lower in concentration but wider in the extent of the individual hot spots, which are already slightly overestimated in Fig. 5c. The first/second effect will improve/worsen, respectively, the agreement with the measurements in Fig. 5a. For an anisotropic diffusion, the dye distribution also depends on the direction of the fastest spreading and anisotropy ratio in addition to the diffusivity magnitude. Note also that spatially dependent diffusivities may still be needed to more accurately capture the effects of the small-scale motions. In the near field, the agreement with observations is still marginal because, as mentioned above, the eddy diffusivity concept is not designed to represent the effects of the individual features over short time scales but rather the overall eddy-induced spreading of the dye over longer time intervals.

d. *Comparing the spread of pseudotrajectories to the spread of real drifter trajectories*

It is interesting to compare the spreading of pseudotrajectories (that were used to estimate the radar-specific eddy diffusivity tensor in section 3b) with the spreading of the real drifter trajectories. For a fair comparison, we computed the spreading of real drifters on similar spatial scales as for the pseudodrifters, where separations between real drifters do not exceed 1.5 km. For the August experiment, the real drifter–based dispersion tensor (shown in Fig. 10) grows with time faster than the pseudotrajectory-based dispersion tensor (Fig. 8) and reaches the limiting scale of 2 km^2 in less than 5 h (while pseudotrajectory dispersion had barely reached 1 km^2 after 8 h). Interestingly, the angle of the fastest spreading ($\theta = 66°$) and the spread in the minor axis direction are comparable for the pseudotrajectories and real trajectories. The dispersion in the direction of the fastest spreading is, on the other hand, about 3 times larger for the full trajectories than for pseudotrajectories, suggesting that even though the radar does not fully resolve the motions at scales below 1.5 km, it still represents a significant portion of the variability of the total velocity field at those scales. This variability appears to contribute significantly to the spread of real drifters but is eliminated when computing pseudotrajectories. The fast spreading of the real drifters is largely ballistic and is caused by the mean velocity shear elongating the drifter patch. To illustrate this, we have estimated the slopes of the D versus t curve on a logarithmic scale (Fig. 10b), which are 1.9 and 1.7 in the major and minor directions, respectively. This confirms that the spread of real drifters at the considered spatial scales is closer to a ballistic process (slope of 2) than to diffusion (slope of 1). Consistent with this interpretation, the real drifter–based dispersion curve in the direction of the fastest spreading (blue dotted curve in Fig. 10a) agrees well with the theoretically predicted ballistic spreading $D_{\text{ballistic}} = (|d\mathbf{V}/d\mathbf{x}|\Delta x t)^2$ (blue dashed curve in Fig. 10a), where the velocity shear magnitude $|d\mathbf{V}/d\mathbf{x}| \approx 3 \times 10^{-5}\,\text{s}^{-1}$ was estimated numerically from the radar velocities at the time and location of the August drifter deployment, and $\Delta x = 3$ km corresponds to

the size of the initial drifter patch. The spreading of real drifters in Fig. 10 is different, less diffusive, and more ballistic (i.e., shows a steeper slope) than the spread of pseudodrifters in Fig. 8. Because ballistic spreading is caused by velocity shear, this suggests that the part of the radar-based velocity field that gets eliminated through constructing pseudotrajectories is mostly responsible for the ballistic rather than diffusive spreading. Converting dispersion into diffusivity by estimating the mean slope of the curve formally leads to diffusivity values of $K_\xi = 39\,\mathrm{m^2\,s^{-1}}$ and $K_\eta = 5.1\,\mathrm{m^2\,s^{-1}}$. Note, however, that by doing so we ignore the fact that the spread of real drifters is largely ballistic and instead represent it as a diffusive process.

The comparison between radar-specific, pseudotrajectory-based diffusivity and conventional drifter-based diffusivity for the September drifter experiment (not shown) leads to similar results as in August. The September pseudotrajectory-based estimates for the small-scale, radar-specific diffusivity in the major and minor directions are 11 and $4.1\,\mathrm{m^2\,s^{-1}}$, whereas estimates based on the spread of real drifters give 27 and $7.4\,\mathrm{m^2\,s^{-1}}$, respectively. The direction of the fastest spreading, $\theta = 0°$, was similar for the pseudotrajectories and for the real drifters. Just as in August, in September the diffusivity resulting from the spread of real drifters in the major spreading direction was roughly 2.5 times larger than the pseudotrajectory-based radar-specific diffusivity, and the spreading of the real drifters was closer to a ballistic regime than the spreading of the pseudodrifters. Because the September experiment was carried out during stronger winds than in August, the similar trends in diffusivity for the two experiments suggest that that these results might be specific for the geographical area but do not depend strongly on the wind conditions.

e. *Comparing drifter-based radar-specific eddy diffusivity to other diffusivity estimates*

Perhaps one of the most widely used diffusivity estimates in prior literature has been obtained by Okubo and has been summarized in Okubo's famous diffusivity diagram [Fig. 2 in Okubo (1971)]. For spatial scales of 1 km (10^5 cm), Okubo's diffusivity values are about $1\,\mathrm{m^2\,s^{-1}}$ ($10^4\,\mathrm{cm^2\,s^{-1}}$), which is an order of magnitude smaller than our estimate for K_ξ. This discrepancy could be due to a number of reasons, one possible difference being that our estimates are specific to the Martha's Vineyard inner-shelf area with strong lateral velocity shear and strong tidal currents that generate small-scale variability in the flow through interaction with bathymetry, whereas Okubo's values were obtained by combining data from various experiments in different regions of the World Ocean. To investigate the importance of using a proper diffusivity estimate, we recomputed the predicted dye distributions using the isotropic $1\,\mathrm{m^2\,s^{-1}}$ Okubo diffusivity instead of drifter-based radar-specific anisotropic diffusivity superimposed on the radar fields. The results are shown in Figs. 9c(1)–9c(4), 10, and 5d. As expected, this smaller value of diffusivity led to less spreading of the dye and resulted in a more compact dye distribution (Fig. 5d). The Rhd predictions were overly concentrated, exceeding observations by more than a factor of 4 at many locations along the ship track (Fig. 5d). In addition, the smaller diffusivity value did not widen the dye distribution enough to produce the fourth easternmost hot spot observed during the survey. Overall, using Okubo diffusivity improved the predicted dye distribution compared to the no diffusion case, but the improvements were not as striking as in the simulations with the drifter-based radar-specific diffusivity.

Finally, the diffusivity over small spatiotemporal scales could also be estimated from the aerial images of the dye taken by the quadcopter-mounted digital camera during the dye release (Fig. 3). More specifically, assuming that the widening of the streak of dye is entirely due to diffusive process, the diffusivity could be estimated using Eq. (2) from the difference between the initial streak width and the streak width at some later time as

$$
\begin{aligned}
K &= \frac{1}{2}\frac{\partial D}{\partial t} \approx \frac{1}{2}\frac{[l^2_{\mathrm{streak}}(t_1) - l^2_{\mathrm{streak}}(t_0)]}{t_1 - t_0} \\
&\approx \frac{l^2_{\mathrm{streak}}(t_0)}{2(t_1 - t_0)}\left\{\left[\frac{l_{\mathrm{streak}}(t_1)}{l_{\mathrm{streak}}(t_0)}\right]^2 - 1\right\} \\
&\approx \frac{(5.2\,\mathrm{m})^2}{2\times 9\,\mathrm{min}}(15^2 - 1) \approx 5.6\,\mathrm{m^2\,s^{-1}}.
\end{aligned}
$$

Here, the initial streak width at t_0 was taken to be the width of R/V *Tioga*'s beam (5.2 m), and the streak width 9 min later was determined from the pixel count at location A [leading to $l_{\mathrm{streak}}(t_1)/l_{\mathrm{streak}}(t_0) \approx 15$], where the ship passed approximately 9 min prior to the time of the photo snapshot on the georectified photograph that has been corrected for the height and angle of the camera and camera lens distortion. This back-of-the-envelope estimate of diffusivity is 2.7 times smaller than our drifter-based estimate for K_ξ, slightly larger than our estimate for K_η, and more than 5 times larger than Okubo's estimate. It is interesting that the image-based estimate of diffusivity during the initial stages of dye spreading is comparable to the larger-scale drifter-based diffusivity estimated over several hours. Possibly, this is due to the ship's wake effect that could be a major player in enhancing the short-term initial diffusion of the dye.

Because the image-based diffusivity is between the Okubo estimate and our drifter-based estimate, numerical simulations with these early, tracer-based diffusivities were not carried out in this study.

4. Summary and conclusions

The eddy diffusivity approach to parameterizing subgrid-scale motions in numerical or data-based ocean models became widely popular due to its simplicity and computational efficiency. However, the validity and applicability of this approach to the real ocean is not obvious and requires more thorough testing. In this paper, we have investigated how well the concept of eddy diffusivity performs in the coastal ocean by making use of a unique dataset from a field experiment that took place in August 2014 south of Martha's Vineyard, Massachusetts. The term eddy diffusivity is used here to denote the action of small-scale motions that are unresolved and underresolved by the radar. More specifically, we used real drifter data from the experiment to estimate eddy diffusivity and then incorporated this diffusivity-based parameterization into a radar-based advection model to simulate the spreading of dye in the coastal ocean. The results were compared to observed dye distributions from a field experiment to quantify the performance of this approach.

In our analysis, we made use of the concept of a scale-dependent and model-specific diffusivity, which allows parameterizing the effects of unresolved and underresolved motions that are not properly represented by the model, rather than parameterizing the entire eddy field. Our results suggest that incorporating drifter-based diffusivity greatly improves the performance of the radar in reproducing the observed movement and spreading of the dye. The obtained diffusivity values are $O(10)\,\mathrm{m^2\,s^{-1}}$, are consistent with the diffusivity inferred from aerial images of the dye taken using the quadcopter-mounted digital camera during the dye release, and are roughly an order of magnitude larger than diffusivity estimates of Okubo [$O(1)\,\mathrm{m^2\,s^{-1}}$] for similar spatial scales ($\sim$1 km). Predicted dye distributions in simulations with drifter-based, radar-specific anisotropic diffusivity were shown to have better agreement with data than those resulting from simulations with isotropic Okubo diffusivity. The significance of the anisotropy and the importance of the spatial variability of the eddy diffusivities were not specifically evaluated here.

Finally, we have used radar and drifter data from the second part of the field experiment that took place in the same geographical area in September 2014, a month later than the main experiment, to look at the temporal variability in the diffusivity estimates. The August and September diffusivity estimates were consistent with each other (same order of magnitude), despite the fact that wind was much stronger during the September release and the resulting drifter trajectories were quite different between the two experiments. This indicates that diffusivity in the coastal ocean might not be strongly dependent on the wind conditions and could instead be dominated by tidally and/or topographically driven processes. However, further investigation is required to confirm this. Differences in eddy diffusivities between the inner shelf of Martha's Vineyard and other coastal regions also present an open question.

Acknowledgments. IR, AK, and SL were supported by the NSF OCE Grant 1332646. IR was also supported by NASA Grant NNX14AH29G. We thank Jim Ledwell for his help and guidance in planning and carrying out the dye release experiments and for his comments on this manuscript; Peter Traykovski for providing help with obtaining, processing, rectifying, and interpreting aerial photos of the dye taken by the quadcopter-mounted digital camera; Brian Guest for help with the dye release and dye surveys; the captain and crew of R/V *Tioga* for their excellent performance during the field experiment; and graduate students from the joint WHOI/MIT program for assisting with drifter release and recovery.

REFERENCES

Abernathey, R. P., and J. Marshall, 2013: Global surface eddy diffusivities derived from satellite altimetry. *J. Geophys. Res. Oceans*, **118**, 901–916, doi:10.1002/jgrc.20066.

Bennett, A. F., 1984: Relative dispersion: Local and nonlocal dynamics. *J. Atmos. Sci.*, **41**, 1881–1886, doi:10.1175/1520-0469(1984)041<1881:RDLAND>2.0.CO;2.

Beron-Vera, F. J., and J. H. LaCasce, 2016: Statistics of simulated and observed pair separation in the Gulf of Mexico. *J. Phys. Oceanogr.*, doi:10.1175/JPO-D-15-0127.1, in press.

Chen, C., and Coauthors, 2014: Process modeling studies of physical mechanisms of the formation of an anticyclonic eddy in the central Red Sea. *J. Geophys. Res. Oceans*, **119**, 1445–1464, doi:10.1002/2013JC009351.

Chen, R., J. L. McClean, S. Gille, and A. Griesel, 2014: Isopycnal eddy diffusivities and critical layers in the Kuroshio Extension from an eddying ocean model. *J. Phys. Oceanogr.*, **44**, 2191–2211, doi:10.1175/JPO-D-13-0258.1.

Davis, R. E., 1991: Observing the general circulation with floats. *Deep-Sea Res.*, **38**, 531–571, doi:10.1016/S0198-0149(12)80023-9.

Griesel, A., S. T. Gille, J. Sprintall, J. L. McClean, J. H. LaCasce, and M. E. Maltrud, 2010: Isopycnal diffusivities in the Antarctic Circumpolar Current inferred from Lagrangian floats in an eddying model. *J. Geophys. Res.*, **115**, C06006, doi:10.1029/2009JC005821.

Kamenkovich, I., I. I. Rypina, and P. Berloff, 2015: Properties and origins of the anisotropic eddy-induced transport in

the North Atlantic. *J. Phys. Oceanogr.*, **45**, 778–791, doi:10.1175/JPO-D-14-0164.1.

Kirincich, A. R., 2016: The occurrence, drivers, and implications of submesoscale eddies on the Martha's Vineyard inner shelf. *J. Phys. Oceanogr.*, doi: 10.1175/JPO-D-15-0191.1, in press.

——, T. de Paolo, and E. Terrill, 2012: Improving HF radar estimates of surface currents using signal quality metrics, with application to the MVCO high-resolution radar system. *J. Atmos. Oceanic Technol.*, **29**, 1377–1390, doi:10.1175/JTECH-D-11-00160.1.

——, S. Lentz, J. Farrar, and N. Ganju, 2013: The spatial structure of tidal and mean circulation over the inner shelf south of Martha's Vineyard, Massachusetts. *J. Phys. Oceanogr.*, **43**, 1940–1958, doi:10.1175/JPO-D-13-020.1.

LaCasce, J. H., 2008: Statistics from Lagrangian observations. *Prog. Oceanogr.*, **77**, 1–29, doi:10.1016/j.pocean.2008.02.002.

——, and C. Ohlmann, 2003: Relative dispersion at the surface of the Gulf of Mexico. *J. Mar. Res.*, **61**, 285–312, doi:10.1357/002224003322201205.

Molcard, A., P. Poulain, P. Forget, A. Griffa, Y. Barbin, J. Gaggelli, J. C. De Maistre, and M. Rixen, 2009: Comparison between VHF radar observations and data from drifter clusters in the Gulf of La Spezia (Mediterranean Sea). *J. Mar. Syst.*, **78**, S79–S89, doi:10.1016/j.jmarsys.2009.01.012.

Nakamura, N., 1996: Two-dimensional mixing, edge formation, and permeability diagnosed in the area coordinate. *J. Atmos. Sci.*, **53**, 1524–1537, doi:10.1175/1520-0469(1996)053<1524:TDMEFA>2.0.CO;2.

——, 2001: A new look at eddy diffusivity as a mixing diagnostic. *J. Atmos. Sci.*, **58**, 3685–3701, doi:10.1175/1520-0469(2001)058<3685:ANLAED>2.0.CO;2.

Ohlmann, C., P. White, L. Washburn, E. Terrill, B. Emery, and M. Otero, 2007: Interpretation of coastal HF radar–derived surface currents with high-resolution drifter data. *J. Atmos. Oceanic Technol.*, **24**, 666–680, doi:10.1175/JTECH1998.1.

Okubo, A., 1971: Oceanic diffusion diagram. *Deep-Sea Res. Oceanogr. Abstr.*, **18**, 789–802, doi:10.1016/0011-7471(71)90046-5.

Poje, A. C., and Coauthors, 2014: Submesoscale dispersion in the vicinity of the Deepwater Horizon spill. *Proc. Natl. Acad. Sci. USA*, **111**, 12 693–12 698, doi:10.1073/pnas.1402452111.

Poulain, P.-M., R. Gerin, and E. Mauri, 2009: Wind effects on drogued and undrogued drifters in the eastern Mediterranean. *J. Atmos. Oceanic Technol.*, **26**, 1144–1156, doi:10.1175/2008JTECHO618.1.

Richardson, L. F., 1926: Atmospheric diffusion on a distance-neighbour graph. *Proc. Roy. Soc. London*, **A110**, 709–737, doi:10.1098/rspa.1926.0043.

Rypina, I. I., L. J. Pratt, J. Pullen, J. Levin, and A. Gordon, 2010: Chaotic advection in an archipelago. *J. Phys. Oceanogr.*, **40**, 1988–2006, doi:10.1175/2010JPO4336.1.

——, I. Kamenkovich, P. Berloff, and L. J. Pratt, 2012: Eddy-induced particle dispersion in the near-surface North Atlantic. *J. Phys. Oceanogr.*, **42**, 2206–2228, doi:10.1175/JPO-D-11-0191.1.

——, A. R. Kirincich, R. Limeburner, and I. A. Udovydchenkov, 2014: Eulerian and Lagrangian correspondence of high-frequency radar and surface drifter data: Effects of radar resolution and flow components. *J. Atmos. Oceanic Technol.*, **31**, 945–966, doi:10.1175/JTECH-D-13-00146.1.

Sallee, J.-B., K. Speer, R. Morrow, and R. Lumpkin, 2008: An estimate of Lagrangian eddy statistics and diffusion in the mixed layer of the Southern Ocean. *J. Mar. Res.*, **66**, 441–463, doi:10.1357/002224008787157458.

Stewart, R., and J. Joy, 1974: HF radio measurements of surface currents. *Deep-Sea Res. Oceanogr. Abstr.*, **21**, 1039–1049, doi:10.1016/0011-7471(74)90066-7.

Sundermeyer, M., and J. Ledwell, 2001: Lateral dispersion over the continental shelf: Analysis of dye release experiments. *J. Geophys. Res.*, **106**, 9603–9621, doi:10.1029/2000JC900138.

Zhurbas, V., and I. S. Oh, 2004: Drifter-derived maps of lateral diffusivity in the Pacific and Atlantic Oceans in relation to surface circulation patterns. *J. Geophys. Res.*, **109**, C05015, doi:10.1029/2003JC002241.